Research Article Vol. 10, No. 11 / November 2023 / Optica 1535

Mid-infrared spectroscopy with a broadly tunable thin-film lithium niobate optical parametric oscillator

Alexander Y. Hwang,[1] Hubert S. Stokowski,[1] Taewon Park,[1] Marc Jankowski,[2] Timothy P. McKenna,[2] Carsten Langrock,[1] Jatadhari Mishra,[1] Vahid Ansari,[1] Martin M. Fejer,[1] and Amir H. Safavi-Naeini[1,*]

[1]E.L. Ginzton Laboratory, Stanford University, Stanford, California 94305, USA
[2]Physics & Informatics Laboratories, NTT Research, Inc., Sunnyvale, California 94085, USA
*safavi@stanford.edu

Received 7 August 2023; revised 11 October 2023; accepted 13 October 2023; published 15 November 2023

Mid-infrared spectroscopy, an important technique for sensing molecules, has encountered barriers from sources either limited in tuning range or excessively bulky for widespread use. We present a compact, efficient, and broadly tunable optical parametric oscillator surmounting these challenges. Leveraging dispersion-engineered thin-film lithium niobate-on-sapphire photonics and a singly resonant cavity allows broad, controlled tuning over an octave from 1.5–3.3 μm. The device generates >25 mW of mid-infrared light at 3.2 μm with 15% conversion efficiency. The ability to precisely control the device's mid-infrared emission enables spectroscopy of methane and ammonia, demonstrating our approach's relevance for sensing. Our work signifies an important advance in nonlinear photonics miniaturization, bringing practical field applications of high-speed, broadband mid-infrared spectroscopy closer to reality.

https://doi.org/10.1364/OPTICA.502487

1. INTRODUCTION

A fundamental technique for sensing is mid-infrared (MIR) spectroscopy, which exploits molecules' strong and distinct absorption responses in the 2–20 μm spectral region. High-sensitivity and high-resolution MIR spectroscopy with coherent sources has rich applications, e.g., in gas [1], chemical reaction [2], and biological [3] sensing. Further advancing broadband, field-deployable MIR sources would enable a multitude of applications in areas such as rapid portable health monitoring and wide-coverage greenhouse gas detection.

However, currently available sources still suffer from significant limitations. For instance, compact quantum- and interband-cascade lasers have dramatically improved their output power and efficiency, making them prominent sources for MIR spectroscopy [4]. However, material-defined gain bandwidths restrict tuning to hundreds of cm^{-1} [5], limiting potential multi-species detection. Meanwhile, optical parametric oscillator (OPO) sources allow efficient conversion of low-noise, wavelength-agile near-IR lasers over extremely broad tuning ranges (often thousands of cm^{-1}) [6–8]. However, their conventional use of bulk optics creates large footprints, high threshold powers, high cost, and demanding stabilization requirements. These factors limit widespread field applications of OPOs, despite many laboratory spectroscopic studies [6].

Because of the limitations of bulk systems, OPO miniaturization has been actively pursued. Well-established systems include integrated weakly confining waveguide cavities [9], polished crystals [10], and whispering-gallery resonators [11]. Moreover, recent nanofabrication breakthroughs have led to on-chip planar nanophotonic circuits in strongly nonlinear materials such as lithium niobate (LN). Sub-wavelength transverse mode confinement in these architectures allows enhanced nonlinear efficiency [12,13], dispersion engineering for ultrabroadband operation [14–16], and capability for complex nonlinear photonic circuits [17]. As a result, the first on-chip OPOs integrated with highly scalable, small-footprint, nanophotonic circuits have recently been developed [18–23].

Despite these rapid advances, recent nanophotonic integrated OPOs thus far have limited capability for MIR spectroscopy. One reason for this is that established nonlinear integrated photonic platforms utilize a silica undercladding that becomes strongly absorptive past 3 μm [24], limiting MIR performance. Another crucial reason is that engineering nanophotonic OPOs with sufficiently stable and precise tuning over fine spectroscopic lines is challenging. Bulk OPO-based spectroscopy systems usually achieve ideal tuning behavior by engineering the cavity in a singly resonant configuration with a resonant signal wave and non-resonant, freely tunable MIR idler wave [6,7,25–28]. Developing such wavelength-selective behavior within a high-quality-factor nanophotonic cavity is non-trivial. This has led previous integrated

OPOs to simultaneously resonate signal and idler beams in either doubly [20,21] or triply resonant [18,19,22,23] configurations, creating complex tuning dynamics undesirable for spectroscopy.

Here we demonstrate an efficient, broadly tunable, continuous-wave integrated MIR OPO and use it for gas spectroscopy. This single-wavelength MIR source complements broadband integrated MIR frequency comb sources [29–36] that can exhibit more complex dynamics, difficult calibration/stabilization, low efficiency, and limited resolution. Pumped with continuous-wave light at $\lambda_p = 1$ μm, a single dispersion-engineered device exhibits broad tuning over an octave from 1.5–3.3 μm. By engineering a wavelength-selective, high-quality-factor cavity, we realize pump-enhanced singly resonant MIR OPO operation. The OPO's reliable tuning behavior allows us to measure the spectra of methane and ammonia, demonstrating the spectrosopic potential of OPOs within a fully chip-integrated platform. We discuss clear paths towards further enhancing the current OPO for widespread, practical use by improving overall system efficiency, near-degenerate performance, and gap-free tuning range.

2. RESULTS

A. Device Concept and Operation

Figure 1(a) illustrates our OPO design. An optical cavity incorporates an $\chi^{(2)}$ nonlinear crystal that provides parametric amplification between $\lambda_p = 1$ μm pump light and generated signal/idler light at $\lambda_s = 1.5$ μm and $\lambda_i = 3$ μm [Fig. 1(a.i)]. We design the cavity to be strongly resonant for λ_s, weakly resonant for λ_p, and non-resonant for λ_i, classifying it as a pump-enhanced singly resonant OPO (SRO) [26]. This design allows the MIR idler to freely tune for spectroscopy. An effective, simple SRO fine tuning method [6,7,25,37] sweeps λ_p while λ_s clamps on a strong cavity resonance, so λ_i tunes freely by energy conservation, e.g., over molecular absorption peaks [Fig. 1(a.ii)]. Tuning the temperature and pump wavelength broadly adjusts the OPO output over 1.5–3.3 μm [Fig. 1(a.iii)], which overlaps fundamental vibrational transitions of dozens of small molecules (e.g., CO_2, CH_4, H_2O, and NH_3) important for spectroscopic monitoring.

We implement the integrated OPO device [Fig. 1(b)] in a photonic circuit composed of etched LN-on-sapphire ridge waveguides. Deeply etched LN-on-sapphire photonics, with substrate transparency up to 4.5 μm, have enabled dispersion-engineered broadband MIR generation up to 4 μm [24,38]. We fabricate 15 OPOs with different design parameters on a 12 × 12 mm LN-on-sapphire chip [Fig. 1(b.i)], then focus on the optimal device for the experiment. Periodically poling one of the LN waveguides over 9.3 mm [Fig. 1(b.ii)] compensates for phase-velocity mismatch and allows broadband parametric gain. We choose the parametric gain waveguide geometry (875 nm LN film, 600 nm etch, and 1.95 μm top width) to enable strong fundamental transverse electric mode confinement at pump/signal/idler wavelengths [Fig. S1(a)] and large parametric gain from modal overlap. Moreover, choosing this geometry produces ultrabroadband gain at degeneracy from near-zero signal/idler group velocity dispersion (GVD) (see Section 2.C and Supplement 1, Section 7). We fabricate waveguide devices by patterning HSQ resist with 100 kV electron-beam lithography, then etching with Ar ion milling (more details in Supplement 1, Section 2).

The pump-enhanced SRO cavity combines waveguide bends with two crucial engineered elements: the output coupler and intracavity coupler. The output coupler [Fig. 1(b.iii)] is a directional coupler designed for 70%–100% transfer of MIR light ($\lambda_i > 3$ μm) out of the cavity while only extracting ∼1% of telecom signal light (1.5 μm $< \lambda_i <$ 1.7 μm). The intracavity coupler is an adiabatic coupler designed for broadband, ∼100% transfer of telecom-wavelength light to enable strong signal resonances. In Supplement 1, Section 1, we show design details and simulated power coupling versus wavelength for the output coupler [Fig. S1(b), (c)] and intracavity coupler [Fig. S1(d), (e)]. To verify the strong cavity modes at λ_s, we sweep resonances with a tunable telecom laser [Fig. S3(a)], revealing sharp, low-loss signal modes with total quality factor $Q_{tot} = 1.3-1.6 \times 10^6$ [Fig. 1(c)]. This corresponds to ≈ 12% round-trip loss in the 22.3 mm long cavity. Extracted intrinsic/extrinsic Q-factors for the undercoupled cavity are $Q_i = 1.35-1.7 \times 10^6$ and $Q_{ex} \approx 20 \times 10^6$, respectively. High Q-factors extend over our telecom laser's whole tuning range [1500–1640 nm, Fig. S3(b)]. Meanwhile, the 1 μm pump

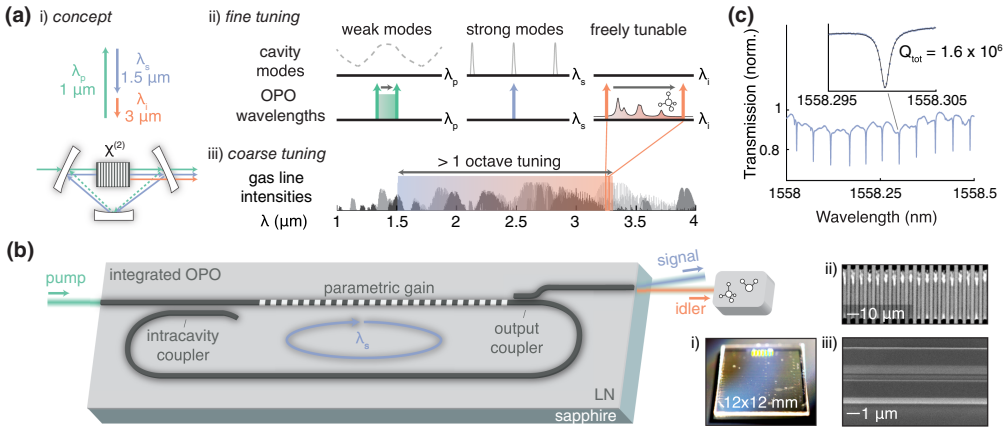

Fig. 1. OPO concept and design. (a) Inset (i): diagram of a pump-enhanced SRO operating at 1/1.5/3 μm. Inset (ii): cavity designed to strongly resonate the signal, weakly resonate the pump, and leave the idler free to tune continuously for MIR spectroscopy. Inset (iii): wide coarse tunability of single integrated OPO overlayed on spectral line intensities (log scale) for CH_4, H_2O, N_2O, CO_2, and NH_3 versus wavelength. (b) Schematic of the on-chip integrated pump-enhanced SRO on LN-on-sapphire photonics. Inset (i): image of fabricated 12 × 12 mm chip containing 15 devices. Inset (ii): second harmonic generation microscopy image of periodically poled domains. Inset (iii): scanning electron micrograph of waveguide coupler. (c) High-quality-factor resonant modes for signal wavelengths near 1550 nm. Inset: Lorentzian fit for single mode at 1558.3 nm.

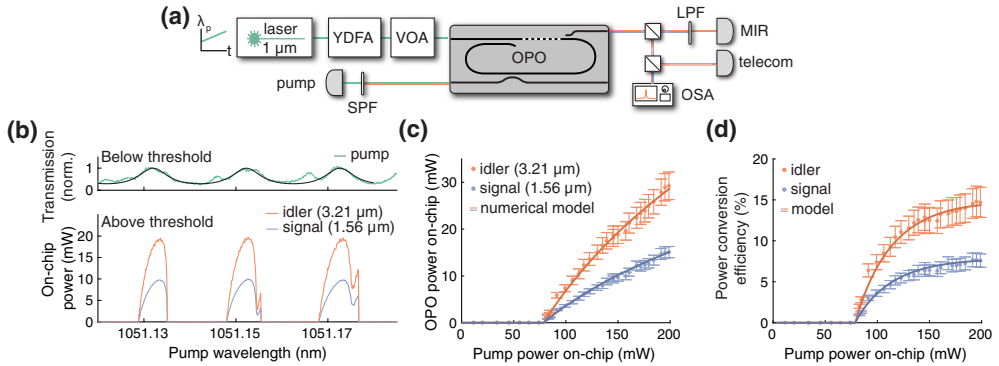

Fig. 2. OPO power and efficiency. (a) Simplified diagram of measurement setup for power and spectral characterization (full diagram in Fig. S2, Supplement 1). YDFA, ytterbium-doped fiber amplifier; VOA, variable optical attenuator; LPF, long-pass filter; SPF, short-pass filter; OSA, optical spectrum analyzer. (b) Top panel: normalized pump transmission below threshold ($P_{\text{pump}} = 45$ mW) reveals low-finesse pump resonances with Airy function fit to a finesse of 2.4 (see Supplement 1, Section 4). Bottom panel: OPO output powers versus pump wavelength, at $P_{\text{pump}} = 157$ mW on-chip. (c) Output on-chip powers and (d) power conversion efficiency versus pump power. Error bars come from uncertainty in fiber-chip and chip-detector collection efficiency (see Supplement 1, Section 3). Solid lines from numerical modeling of the pump-enhanced SRO.

only weakly resonates, with cavity finesse $F = 2.5-3.5$, corresponding to ≈11% total power recirculation and 2× intracavity power enhancement (Fig. S4).

To operate the device, we couple continuous-wave pump light onto the chip using a Hi1060 single-mode lensed fiber with (33 ± 2)% coupling efficiency (Supplement 1, Section 3B). When parametric gain provided by the pump exceeds round-trip signal loss, the device oscillates, generating signal and idler photons. We collect output light using a zinc fluoride glass multimode fiber (La Verre Fluoré) with ∼3% MIR chip-to-fiber collection efficiency (Supplement 1, Section 3D), and the idler beam is used for MIR spectroscopy [Fig. 1(b)]. We attribute the few-percent chip-to-fiber collection efficiency to the roughly cleaved output fiber facet and mismatch between a high-NA LN waveguide and NA = 0.2 fiber. Chip–fiber and fiber–chip coupling efficiencies could be improved dramatically to 80%–90% using cladding mode-matching waveguides [39–41] and/or placing a high-NA lens on the output (>70%−80% efficiency measured on a different chip/setup).

Figure 2(a) depicts the optical measurement setup built around the device used for basic characterization (more details in Supplement 1, Section 3 and Fig. S2). Continuous-wave 1 μm pump light comes from an external cavity diode laser (Toptica DL Pro) amplified by an ytterbium-doped fiber amplifier (Civil Laser) with 1040–1090 nm operating bandwidth. We monitor the pump wavelength using a wavelength meter (Bristol Instruments Model 621). Device output emission collected in the MIR multimode fiber is collimated then routed to a HgCdTe MIR detector (Thorlabs PDAVJ5), InGaAs telecom-band detector (Newport 1623), and an optical spectrum analyzer (Yokogawa AQ6376). We measure pump light cavity transmission by collecting with a silica multimode fiber (Thorlabs FP200ERT) and measuring with an InGaAs detector (Newport 1623). The entire chip is heated with a cartridge heater and temperature-stabilized (mean temperature fluctuations ∼0.1°C) with a thermoelectric cooler.

B. Power Characterization

We tune the device to 170°C and pump near $\lambda_p = 1.051$ μm to obtain clean non-degenerate parametric oscillation at $\lambda_s = 1.56$ μm, $\lambda_i = 3.21$ μm. Because of weak pump resonances [Fig. 2(b), top], intracavity pump intensity, and hence generated signal/idler output [Fig. 2(b), bottom], varies periodically with λ_p. Because the pump resonance is weak, tuning to a specific λ_p leads to stable continuous-wave oscillation for >10−15 min without any cavity or laser stabilization [Fig. S5(a)].

We then scan λ_p for different pump powers and record maximum generated signal/idler powers. We observe clear pump depletion but do not precisely quantify it due to background pump light scattering into the multimode collection fiber. The device begins oscillating with 80 ± 6 mW on-chip threshold pump power [Fig. 2(c)]. Above threshold, the generated signal/idler powers monotonically increase with pump power. With ∼200 mW on-chip pump power, the device produces a maximum of 29 ± 3 mW on-chip power at 3.2 μm. This power level has been used for portable sensor systems [42] and exceeds the typical required power for shot-noise-limited MIR detection (∼0.1 mW) [6]. The on-chip power conversion efficiency of signal/idler also increases monotonically within the range of pump power sweeps [Fig. 2(d)]. We measure a maximum of (15 ± 2)% on-chip power conversion efficiency (45% quantum efficiency) from the pump to MIR idler. An ideal OPO produces nearly 100% quantum efficient conversion (≈33% power conversion at these wavelengths) [7]. Our device's deviation is likely caused by modal/radiative scattering of pump light in waveguide tapers (see Supplement 1), MIR losses from, e.g., surface-adsorbed molecules [24,38], and <100% MIR light transfer in the output coupler [see Fig. S1(e)].

The measured dependence of the emitted MIR light on input pump power aligns well with numerical modeling of a weakly pump-enhanced SRO [Figs. 2(c) and 2(d), solid lines], verifying that the device behaves as designed. In our modeling (Supplement 1, Section 5) we assume the measured values of total Q-factor (1.6 million), pump recirculation (11%, Supplement 1, Section 4), and normalized efficiency [40%/(W · cm^2), Supplement 1, Section 3C]. The numerically modeled on-chip idler output powers are scaled by 0.46 to account for the effective MIR extraction efficiency, and intracavity signal powers are scaled by 0.013 to account for the intended small (∼1%) signal extraction from the cavity.

C. Tunability

1. Coarse Tunability

We tune our OPO's output wavelength over an octave of bandwidth using a combination of temperature and pump wavelength [Figs. 3(a) and 3(b)]. For each temperature, we measure optical spectra for each pump wavelength tuned coarsely in 2–5 nm steps within the amplifier bandwidth. At the higher temperatures of 100°–200°C, we access the "far-from-degenerate" regime with widely separated signal and idler ($\lambda_s = 1.5-1.7$ μm, $\lambda_i = 3-3.3$ μm) [Fig. 3(a)]. We observe sufficiently reliable tuning for spectroscopy at these operating temperatures and clean output spectra [Fig. 3(b)]. In this wavelength range, the device most often oscillates single-mode, which we verify using high-resolution optical spectra and RF measurements (Fig. S7). The MIR idler must then be single-moded because the pump and telecom signal are both single-moded. In the far-from-degenerate regime, we measure MIR output wavelengths up to 3.315 μm at 200°C, limited by the temperature control range and pump amplifier bandwidth. The high operation temperature is only due to phase matching in this device; future devices can extend deeper into the MIR at lower temperatures by lithographically defining a different poling period. In our device, lower temperatures from 70°–90°C access the "near-degenerate" regime (1.7 μm $< \lambda_s, \lambda_i <$ 2.7 μm), exhibiting broad bandwidths and tunability but also some complex multimoded behavior. Here, multiple optical spectra are taken for each coarse pump wavelength step to capture the broad-spanning oscillation. From 80°–100°C, the OPO sometimes oscillates simultaneously in the near-degenerate and far-from-degenerate regimes.

Pump wavelength tuning at a fixed temperature tunes the device reliably and rapidly over a large range [Fig. 3(a)]. From 80°–200°C, the >2.8 μm idler tunes roughly linearly with pump wavelength. The fitted tuning slope $d\lambda_i/d\lambda_p \approx -2$ at higher temperatures and increases to −4.2 at 100°C. This equates to 100–200 nm MIR wavelength tuning at a given temperature with 50 nm of pump tuning.

As we further decrease the temperature, wavelength tunability rapidly increases as the device begins oscillating at near-degenerate signal/idler waveguide modes with near-zero GVD. At 70°C, we operate the device in the anomalous dispersion regime, resulting in a U-shaped tuning curve that spans over 800 nm [Fig. 3(a)] and agrees with simulations [Fig. S6(a)]. Near degeneracy, the accessible gain bandwidth broadens from cancellation of odd-order dispersion, allowing oscillation at multiple different signal/idler pairs [Fig. 3(b)]. At 80°C, the device operates near the signal/idler zero-GVD point, resulting in broadband OPO output spanning 1.3 μm, a bandwidth approaching a full octave, at a single temperature [Figs. 3(c) and 3(d)]. The increasingly broadband near-degenerate OPO as we increase λ_p and approach zero-GVD at $2\lambda_p$ agrees well with simulation [Fig. 3(c)] [43,44]. From $\lambda_p \approx 1075-1090$ nm, the single-device, single-temperature OPO output spans 1.7–2.7 μm. This 65 THz spanning ultrabroadband gain bandwidth matches that of state-of-the-art pulsed-pump dispersion-engineered thin-film-LN parametric amplifiers [16,45]. To fully harness the broadband OPO operation, future devices could employ an on-chip wavelength control element (e.g., [46,47]) rapidly tunable using LN's electro-optic effect and selective of a particular oscillating mode. Full near-degenerate dispersion-engineering details are described in Supplement 1, Section 7.

2. Fine Tunability

We finely tune the SRO's MIR emission wavelength with sufficient control for use in spectroscopy. At a fixed temperature, we tune the pump laser wavelength. For small changes of λ_p, λ_s stays approximately constant without excessive mode hops while the MIR λ_i tunes by energy conservation [Fig. 3(e)]. The vertical gaps visible in these fine tuning curves are caused by weak pump resonance enhancement, not signal mode hops. Typical gap-free tuning

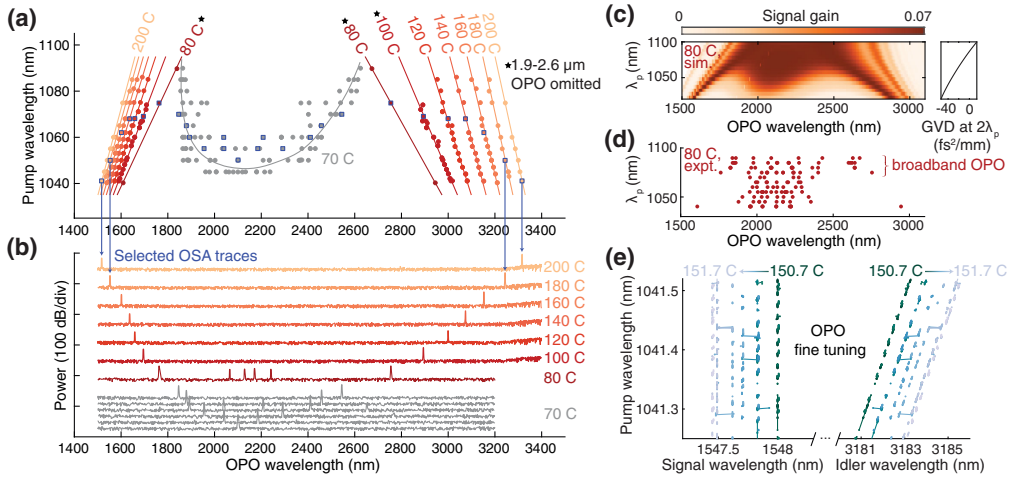

Fig. 3. Coarse and fine tunability. (a) OPO wavelength tuning curves versus λ_p for different temperatures. At 80° and 100°C, the near-degenerate OPO from 1.9–2.6 μm is omitted for clarity [complete data shown in Fig. S6(e)]. At 80°C and above, data are fit to lines, and at 70°C the U-shaped curve is a guide to the eye [simulated tuning in Fig. S6(a)]. Points marked with a blue outline have their output optical spectra plotted in (b). (c), (d) Broadband, 1.3 μm spanning OPO output observed at a single temperature (80°C). (c) OPA gain spectrum simulation, showing degenerate OPO gain bandwidth increasing as λ_p increases and group velocity dispersion (GVD) at degeneracy ($2\lambda_p$) approaches zero. (d) OPO spectral peaks recorded in experiment agree with simulation and exhibit 1 μm OPO span for λ_p near 1075 nm. (e) OPO fine tuning operation: for small changes in λ_p, λ_s stays fixed without excessive mode hops while λ_i increases monotonically, allowing for near-continuous spectral coverage. Gaps in the spectra are due to the weak pump wavelength resonance.

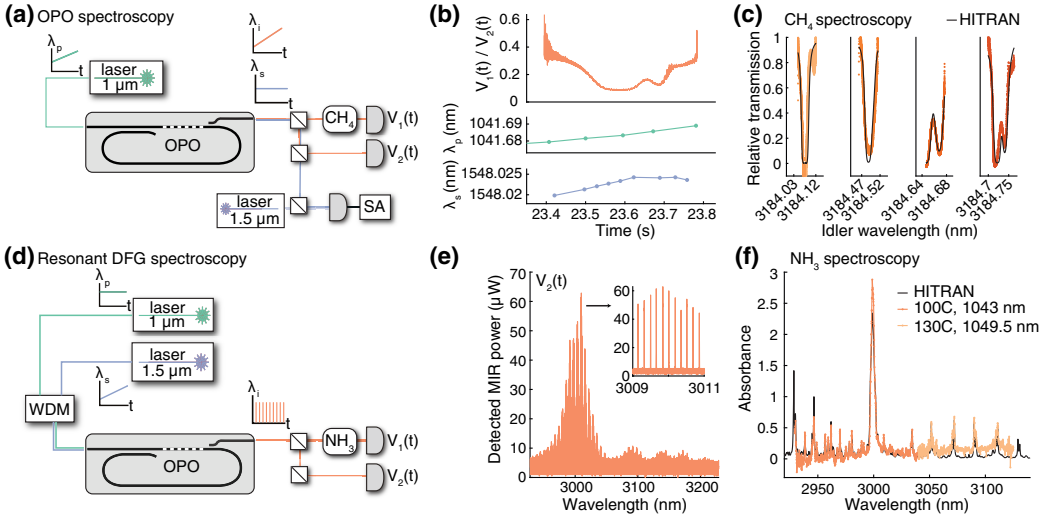

Fig. 4. MIR spectroscopic operation. (a)–(c) OPO spectroscopy of narrow methane lineshapes. (a) Experimental setup showing scanning pump laser input. SA, RF spectrum analyzer. (b) Example trace of measured absorption signal, pump wavelength, and signal wavelength versus time. (c) Methane Doppler-broadened transmission lineshapes for four different scans, compared with data from HITRAN database [48]. (d)–(f) Subthreshold resonant DFG spectroscopy for rapid spectroscopy of broad lineshapes over >100 nm MIR bandwidth. (d) Experimental diagram depicting fixed pump laser input and scanning telecom signal laser. WDM, wavelength division multiplexer. (e) Example trace of output generated MIR signal at detector 2 versus MIR wavelength. (f) Detected MIR absorbance spectrum of ammonia, compared with data from HITRAN database [48].

range is 60–80 pm at 3184 nm (1.8–2.4 GHz), reflecting that the OPO is activated for around one-third of the pump cavity FSR [5.5 GHz, Fig. 2(a)]. Eliminating the weak pump resonance in an optimized fully singly resonant cavity design will allow broader gap-free tuning range. Despite this discontinuous tuning at a fixed temperature, adjusting the chip temperature by only 1°C results in nearly uniform MIR wavelength coverage as different signal modes are selected to oscillate. The signal mode hops when λ_p is detuned sufficiently large amounts [Fig. S8(a)].

D. Proof-of-Concept Spectroscopy

1. OPO Spectroscopy of Methane

We direct part of the output idler light to a low-pressure (20 Torr) methane gas cell (7.5 cm length, Triad Technologies) to measure its absorption spectrum [Fig. 4(a)]. Tuning the device to 151°C with $\lambda_p \approx 1041$ nm shifts the OPO idler output to a cluster of methane absorption lines at 3184 nm. To sweep the generated MIR output over the methane lines, we sweep λ_p in a narrow range [Fig. 4(a)]. During this measurement, the OPO output signal wavelength λ_s stays nearly constant, while the idler wavelength λ_i increases with time [Fig. 4(a)]. The portion of the MIR light passing through the methane cell couples into a photodiode, generating the voltage signal $V_1(t)$. The reference beam of MIR light couples into a second photodiode, generating a reference signal $V_2(t)$. We plot an example trace of the unprocessed relative gas cell transmission scan $V_1(t)/V_2(t)$ in Fig. 4(b), which scans over two absorption peaks.

To calibrate the wavelength axis $\lambda_i(t)$ of the swept MIR beam, we measure $\lambda_p(t)$ and $\lambda_s(t)$ and infer $\lambda_i(t)$ by energy conservation. This method allows us to use precise and more readily available near-IR wavelength measurement tools to infer MIR emission properties. We measure $\lambda_p(t)$ with a wavemeter in the input path [Fig. 4(b)]. Meanwhile, $\lambda_s(t)$ is measured by beating a portion of the generated signal beam against a reference laser (Santec TSL-710) on a 12 GHz fast photodiode (Newport 1554-B). The beatnote is read in an RF spectrum analyzer, from which we extract $\lambda_s(t)$ [Fig. 4(b)]. The observed small (5 pm) redshift of $\lambda_s(t)$ is much smaller than the cavity free spectral range (~45 pm), indicating that the signal mode does not mode hop during this scan, but only shifts slightly, likely due to heating at higher OPO power.

We tune the device to four different absorption transitions of methane near 3184 nm and collect spectra [Fig. 4(c)]. After background subtraction (see Supplement 1, Section 10), collected experimental spectra agree well with HITRAN reference curves [48]. The clean, stable MIR OPO output easily resolves the low-pressure, Doppler-broadened methane peaks with linewidths down to 10 pm/300 MHz/.01 cm^{-1}. This spectral resolution highlights an advantageous aspect of the widely tunable single-wavelength integrated source compared to an integrated frequency comb, which in integrated incarnations has few GHz–100 GHz resolution limited by the cavity free spectral range [29–31,34,35,49–51].

2. Resonant DFG Spectroscopy of Ammonia

In addition to operating as an OPO, the broadband operation and singly resonant nature of our device makes it attractive as a source of MIR light generated by difference frequency generation (DFG). Here, we pump the OPO cavity below threshold, now leaving $\lambda_p(t)$ constant over time [Fig. 4(d)]. We instead seed the device with a scanning telecom-band laser $\lambda_s(t)$. Injected seed builds up strongly when $\lambda_s(t)$ matches a signal cavity resonance and generates a bright MIR idler beam by DFG. Hence, $\lambda_i(t)$ consists of discretely spaced MIR peaks [Fig. 4(d)]. In our device's SRO cavity, peaks at λ_i will be equally spaced in frequency at the signal cavity FSR (≈5.7 GHz) over the entire gain bandwidth. By contrast, in a doubly or triply resonant device, generated MIR peaks would be much more sparse because of the requirement of simultaneous signal and idler resonance. The wide availability of rapidly tunable telecom-band lasers, including on-chip and LN-integrated devices [52–54], makes this resonant DFG technique highly accessible.

We demonstrate the broadband resonant DFG spectroscopy by detecting atmospheric pressure ammonia, which exhibits broad lineshapes with 0.5–10 nm peak widths. As in the methane experiment, the MIR output splits into an ammonia gas cell (1.5 cm length, from Wavelength References) and reference path. We measure λ_p with a wavemeter, assume $\lambda_s(t)$ sweeps linearly with time, then infer $\lambda_i(t)$ by energy conservation. Figure 4(e) shows a typical trace of discrete MIR peaks at detector 2 versus $\lambda_i(t)$, where $\lambda_p = 1043$ nm, and $\lambda_s(t)$ sweeps from 1535 to 1620 nm. Generated equally spaced MIR lines [Fig. 4(e), inset] are strong over an ∼100 nm bandwidth (equates to sweeping λ_s only 30 nm), and the >10 μW MIR output can be detected directly by a DC-coupled photodiode.

By dividing the signal path's discrete peak heights by those from the reference path, we obtain broadband spectra of ammonia with 5 GHz resolution [Fig. 4(f)]. The presented data consist of two scans, each with a high signal-to-noise ratio over 100 nm MIR bandwidth. Adjusting temperature and λ_p tunes the center wavelength of the two scans exactly as the OPO is coarsely tuned [Fig. 3(b)]. We resolve ammonia's narrower features with ∼0.5 nm peak width alongside broader 10 nm peaks in agreement with the HITRAN database.

3. DISCUSSION

In summary, we have designed and implemented an integrated nanophotonic OPO and demonstrated operation for MIR spectroscopy. Such a device inherits the useful advantages of bulk OPOs as MIR spectroscopic light sources (widely available near-IR laser pumps, high efficiency, broad tunability, and high resolution) while adding the benefits of nanophotonic integration (reduced footprint, better stability, lower threshold powers, broadband operation via dispersion engineering, and integration capability). The key enabling advance here is the fabrication of high-quality-factor, wavelength-selective cavities built from the MIR-compatible LN-on-sapphire platform. With the miniaturization of such a useful MIR spectroscopic technology onto a fully chip-integrated platform, a plethora of applications can be envisaged, from deployable gas monitoring systems to portable, real-time MIR biosensors.

Our work outlines a clear path for improving the device sufficiently to realize powerful and deployable sensors. As highlighted in the text, including an electro-optically tunable wavelength-selective intracavity etalon would allow precise, rapid, and low-power control over the broad demonstrated gain bandwidths. The most important factor to improve free-running device stability beyond the observed 10−15 min range would be eliminating the weak pump resonance, by optimizing intracavity coupler design or incorporating better integrated photonic dichronic filter elements with novel design [55] or inverse design [56]. Moreover, incorporating either thermally compensated cavity designs [57] or active electro-optic feedback to reduce output wavelength fluctuations will be important for spectroscopy applications. Operating the device in a quasi-CW fashion with 10% duty cyle pulses results in increased stability >2 h, suggesting that decreasing average power on chip will be beneficial for stability [Fig. S5(b)]. In addition, further gains in efficiency are important and within reach. These will come from improvements in input fiber-to-chip and output chip-to-detector coupling efficiencies. Simulations show that utilizing cladding mode matching waveguides and/or free space optics would raise edge coupling efficiencies to >70%. Moreover, the simulated normalized efficiency is ∼7× larger than the experimentally obtained value (43%/(W · cm^2)), likely due to fabrication imperfections preventing coherent nonlinear enhancement over the full waveguide length. By improving waveguide fabrication we expect threshold powers as low as ∼10 mW, within the output range of heterogeneously integrated lasers near 1 μm [58] and thus potentially enabling full pump-OPO on-chip integration.

Funding. NTT Research; Defense Advanced Research Projects Agency (D19AP00040, HR0011-20-2-0046, RA-18-02-YFA-ES-578); U.S. Department of Energy (DE-AC02-76SF00515); Q-NEXT DOE NQI Center; Air Force Office of Scientific Research (FA9550-17-1-0002); National Science Foundation (2146755, ECCS-2026822); David and Lucile Packard Foundation; Max Planck Institute, Erlangen; Stanford Q-Farm Bloch Fellowship Program; Urbanek Family Fellowship.

Acknowledgment. We thank NTT Research for their financial and technical support. We thank the United States government for their support through the Department of Energy, the Defense Advanced Research Projects Agency (DARPA) LUMOS program, the DARPA Young Faculty Award, and Q-NEXT NQI Center, and the U.S. Air Force Office of Scientific Research MURI. A.Y.H. acknowledges NSF GRFP. H.S.S. acknowledges support from the Urbanek Family Fellowship, and V.A. was partially supported by the Stanford Q-Farm Bloch Fellowship Program and the Max Planck Institute in Erlangen. This work was also performed at the Stanford Nano Shared Facilities (SNSF), supported by the National Science Foundation. We also acknowledge the Q-NEXT DOE NQI Center and the David and Lucille Packard Fellowship for their support. We thank Leo Hollberg for many useful discussions and lending the cells for the gas spectroscopy experiment.

Disclosures. AHS-N, HSS, and AYH are inventors of a patent application that covers the concept and implementation of the integrated optical parametric oscillator and its applications. TP, MJ, TPM, CL, JM, VA, and MMF declare no conflicts of interest.

Data availability. Data underlying the results presented in this paper may be obtained from the authors upon reasonable request.

Supplemental document. See Supplement 1 for supporting content.

REFERENCES

1. G. Ycas, F. R. Giorgetta, E. Baumann, I. Coddington, D. Herman, S. A. Diddams, and N. R. Newbury, "High-coherence mid-infrared dual-comb spectroscopy spanning 2.6 to 5.2 μm," Nat. Photonics **12**, 202–208 (2018).
2. B. Hinkov, F. Pilat, L. Lux, P. L. Souza, M. David, A. Schwaighofer, D. Ristanić, B. Schwarz, H. Detz, A. M. Andrews, B. Lendl, and G. Strasser, "A mid-infrared lab-on-a-chip for dynamic reaction monitoring," Nat. Commun. **13**, 4753 (2022).
3. I. Amenabar, S. Poly, W. Nuansing, E. H. Hubrich, A. A. Govyadinov, F. Huth, R. Krutokhvostov, L. Zhang, M. Knez, J. Heberle, A. M. Bittner, and R. Hillenbrand, "Structural analysis and mapping of individual protein complexes by infrared nanospectroscopy," Nat. Commun. **4**, 2890 (2013).
4. M. S. Vitiello, G. Scalari, B. Williams, and P. De Natale, "Quantum cascade lasers: 20 years of challenges," Opt. Express **23**, 5167–5182 (2015).
5. B. Meng and Q. J. Wang, "Broadly tunable single-mode mid-infrared quantum cascade lasers," J. Opt. **17**, 023001 (2015).
6. M. Vainio and L. Halonen, "Mid-infrared optical parametric oscillators and frequency combs for molecular spectroscopy," Phys. Chem. Chem. Phys. **18**, 4266–4294 (2016).
7. I. Breunig, D. Haertle, and K. Buse, "Continuous-wave optical parametric oscillators: recent developments and prospects," Appl. Phys. B **105**, 99–111 (2011).
8. Y. Kobayashi, K. Torizuka, A. Marandi, R. L. Byer, R. A. McCracken, Z. Zhang, and D. T. Reid, "Femtosecond optical parametric oscillator frequency combs," J. Opt. **17**, 094010 (2015).
9. D. Hofmann, G. Schreiber, W. Grundkotter, R. Ricken, and W. Sohler, "Mid-infrared continuous-wave singly resonant optical parametric oscillator with periodically poled Ti:$LiNbO_3$ waveguide," in *The European Conference on Lasers and Electro-Optics* (2000).

10. C. R. Phillips, J. S. Pelc, and M. M. Fejer, "Continuous wave monolithic quasi-phase-matched optical parametric oscillator in periodically poled lithium niobate," Opt. Lett. **36**, 2973–2975 (2011).
11. N. Amiune, K. T. Zawilski, P. G. Schunemann, K. Buse, and I. Breunig, "Pump tuning of a mid-infrared whispering gallery optical parametric oscillator," Opt. Express **30**, 41084–41091 (2022).
12. R. Luo, Y. He, H. Liang, M. Li, and Q. Lin, "Highly tunable efficient second-harmonic generation in a lithium niobate nanophotonic waveguide," Optica **5**, 1006–1011 (2018).
13. C. Wang, C. Langrock, A. Marandi, M. Jankowski, M. Zhang, B. Desiatov, M. M. Fejer, and M. Lončar, "Ultrahigh-efficiency wavelength conversion in nanophotonic periodically poled lithium niobate waveguides," Optica **5**, 1438–1441 (2018).
14. M. Jankowski, C. Langrock, B. Desiatov, A. Marandi, C. Wang, M. Zhang, C. R. Phillips, M. Lončar, and M. M. Fejer, "Ultrabroadband nonlinear optics in nanophotonic periodically poled lithium niobate waveguides," Optica **7**, 40–46 (2020).
15. M. Jankowski, J. Mishra, and M. M. Fejer, "Dispersion-engineered $\chi^{(2)}$ nanophotonics: a flexible tool for nonclassical light," J. Phys. Photon. **3**, 042005 (2021).
16. L. Ledezma, R. Sekine, Q. Guo, R. Nehra, S. Jahani, and A. Marandi, "Intense optical parametric amplification in dispersion-engineered nanophotonic lithium niobate waveguides," Optica **9**, 303–308 (2022).
17. H. S. Stokowski, T. P. McKenna, T. Park, A. Y. Hwang, D. J. Dean, O. T. Celik, V. Ansari, M. M. Fejer, and A. H. Safavi-Naeini, "Integrated quantum optical phase sensor in thin film lithium niobate," Nat. Commun. **14**, 3355 (2023).
18. T. P. McKenna, H. S. Stokowski, V. Ansari, J. Mishra, M. Jankowski, C. J. Sarabalis, J. F. Herrmann, C. Langrock, M. M. Fejer, and A. H. Safavi-Naeini, "Ultra-low-power second-order nonlinear optics on a chip," Nat. Commun. **13**, 4532 (2022).
19. J. Lu, A. Al Sayem, Z. Gong, J. B. Surya, C.-L. Zou, and H. X. Tang, "Ultralow-threshold thin-film lithium niobate optical parametric oscillator," Optica **8**, 539–544 (2021).
20. A. Roy, L. Ledezma, L. Costa, R. Gray, R. Sekine, Q. Guo, M. Liu, R. M. Briggs, and A. Marandi, "Visible-to-mid-IR tunable frequency comb in nanophotonics," Nat. Commun. **14**, 6549 (2022).
21. L. Ledezma, A. Roy, L. Costa, R. Sekine, R. Gray, Q. Guo, R. Nehra, R. M. Briggs, and A. Marandi, "Octave-spanning tunable infrared parametric oscillators in nanophotonics," Sci. Adv. **9**, eadf9711 (2023).
22. E. F. Perez, G. Moille, X. Lu, J. Stone, F. Zhou, and K. Srinivasan, "High-performance Kerr microresonator optical parametric oscillator on a silicon chip," Nat. Commun. **14**, 242 (2023).
23. X. Lu, A. Chanana, F. Zhou, M. Davanco, and K. Srinivasan, "Kerr optical parametric oscillation in a photonic crystal microring for accessing the infrared," Opt. Lett. **47**, 3331–3334 (2022).
24. J. Mishra, T. P. McKenna, E. Ng, H. S. Stokowski, M. Jankowski, C. Langrock, D. Heydari, H. Mabuchi, M. M. Fejer, and A. H. Safavi-Naeini, "Mid-infrared nonlinear optics in thin-film lithium niobate on sapphire," Optica **8**, 921–924 (2021).
25. A. Henderson and R. Stafford, "Low threshold, singly-resonant CW OPO pumped by an all-fiber pump source," Opt. Express **14**, 767–772 (2006).
26. I. Lindsay, D. Stothard, C. Rae, and M. Dunn, "Continuous-wave, pump-enhanced optical parametric oscillator based on periodically-poled $RbTiOAsO_4$," Opt. Express **11**, 134–140 (2003).
27. M. Vainio, J. Peltola, S. Persijn, F. J. M. Harren, and L. Halonen, "Singly resonant cw OPO with simple wavelength tuning," Opt. Express **16**, 11141–11146 (2008).
28. S. E. Bisson, K. M. Armstrong, T. J. Kulp, and M. Hartings, "Broadly tunable, mode-hop-tuned cw optical parametric oscillator based on periodically poled lithium niobate," Appl. Opt. **40**, 6049–6055 (2001).
29. C. Bao, Z. Yuan, L. Wu, M.-G. Suh, H. Wang, Q. Lin, and K. J. Vahala, "Architecture for microcomb-based GHz-mid-infrared dual-comb spectroscopy," Nat. Commun. **12**, 6573 (2021).
30. A. Shams-Ansari, M. Yu, Z. Chen, C. Reimer, M. Zhang, N. Picqué, and M. Lončar, "Thin-film lithium-niobate electro-optic platform for spectrally tailored dual-comb spectroscopy," Commun. Phys. **5**, 88 (2022).
31. M. Yu, Y. Okawachi, A. G. Griffith, N. Picqué, M. Lipson, and A. L. Gaeta, "Silicon-chip-based mid-infrared dual-comb spectroscopy," Nat. Commun. **9**, 1869 (2018).
32. D. Grassani, E. Tagkoudi, H. Guo, C. Herkommer, F. Yang, T. J. Kippenberg, and C.-S. Brès, "Mid infrared gas spectroscopy using efficient fiber laser driven photonic chip-based supercontinuum," Nat. Commun. **10**, 1553 (2019).
33. H. Guo, C. Herkommer, A. Billat, D. Grassani, C. Zhang, M. H. P. Pfeiffer, W. Weng, C.-S. Brès, and T. J. Kippenberg, "Mid-infrared frequency comb via coherent dispersive wave generation in silicon nitride nanophotonic waveguides," Nat. Photonics **12**, 330–335 (2018).
34. M. Yu, Y. Okawachi, A. G. Griffith, M. Lipson, and A. L. Gaeta, "Microfluidic mid-infrared spectroscopy via microresonator-based dual-comb source," Opt. Lett. **44**, 4259–4262 (2019).
35. K. Luke, Y. Okawachi, M. R. E. Lamont, A. L. Gaeta, and M. Lipson, "Broadband mid-infrared frequency comb generation in a Si_3N_4 microresonator," Opt. Lett. **40**, 4823–4826 (2015).
36. B. Kuyken, T. Ideguchi, S. Holzner, M. Yan, T. W. Hänsch, J. Van Campenhout, P. Verheyen, S. Coen, F. Leo, R. Baets, G. Roelkens, and N. Picqué, "An octave-spanning mid-infrared frequency comb generated in a silicon nanophotonic wire waveguide," Nat. Commun. **6**, 6310 (2015).
37. M. Van Herpen, S. Li, S. Bisson, S. Te Lintel Hekkert, and F. Harren, "Tuning and stability of a continuous-wave mid-infrared high-power single resonant optical parametric oscillator," Appl. Phys. B **75**, 329–333 (2002).
38. J. Mishra, M. Jankowski, A. Y. Hwang, H. S. Stokowski, T. P. McKenna, C. Langrock, E. Ng, D. Heydari, H. Mabuchi, A. H. Safavi-Naeini, and M. M. Fejer, "Ultra-broadband mid-infrared generation in dispersion-engineered thin-film lithium niobate," Opt. Express **30**, 32752–32760 (2022).
39. C. Hu, A. Pan, T. Li, X. Wang, Y. Liu, S. Tao, C. Zeng, and J. Xia, "High-efficient coupler for thin-film lithium niobate waveguide devices," Opt. Express **29**, 5397–5406 (2021).
40. Q. Li, H. Zhang, H. Zhu, Z. Chen, and H. Hu, "Edge coupling for hybrid mono-crystalline silicon and lithium niobate thin films," Opt. Mater. Express **12**, 4147–4154 (2022).
41. T. Zhu, Y. Hu, P. Gatkine, S. Veilleux, J. Bland-Hawthorn, and M. Dagenais, "Ultrabroadband high coupling efficiency fiber-to-waveguide coupler using Si_3N_4/SiO_2 waveguides on silicon," IEEE Photon. J. **8**, 7102112 (2016).
42. F. Sgobba, A. Sampaolo, P. Patimisco, M. Giglio, G. Menduni, A. C. Ranieri, C. Hoelzl, H. Rossmadl, C. Brehm, V. Mackowiak, D. Assante, E. Ranieri, and V. Spagnolo, "Compact and portable quartz-enhanced photoacoustic spectroscopy sensor for carbon monoxide environmental monitoring in urban areas," Photoacoustics **25**, 100318 (2022).
43. Y.-C. Lin, Y. Nabekawa, and K. Midorikawa, "Optical parametric amplification of sub-cycle shortwave infrared pulses," Nat. Commun. **11**, 3413 (2020).
44. A. V. Muraviev, V. O. Smolski, Z. E. Loparo, and K. L. Vodopyanov, "Massively parallel sensing of trace molecules and their isotopologues with broadband subharmonic mid-infrared frequency combs," Nat. Photonics **12**, 209–214 (2018).
45. M. Jankowski, N. Jornod, C. Langrock, B. Desiatov, A. Marandi, M. Lončar, and M. M. Fejer, "Quasi-static optical parametric amplification," Optica **9**, 273–279 (2022).
46. Y. Wang, J. A. Holguín-Lerma, M. Vezzoli, Y. Guo, and H. X. Tang, "Photonic-circuit-integrated titanium:sapphire laser," Nat. Photonics **17**, 338–345 (2023).
47. B. Stern, X. Ji, Y. Okawachi, A. L. Gaeta, and M. Lipson, "Battery-operated integrated frequency comb generator," Nature **562**, 401–405 (2018).
48. I. Gordon, L. Rothman, R. Hargreaves, *et al.*, "The HITRAN2020 molecular spectroscopic database," J. Quant. Spectrosc. Radiat. Transfer **277**, 107949 (2022).
49. Y. Hu, M. Yu, B. Buscaino, N. Sinclair, D. Zhu, R. Cheng, A. Shams-Ansari, L. Shao, M. Zhang, J. M. Kahn, and M. Lončar, "High-efficiency and broadband on-chip electro-optic frequency comb generators," Nat. Photonics **16**, 679–685 (2022).
50. N. Picqué and T. W. Hänsch, "Frequency comb spectroscopy," Nat. Photonics **13**, 146–157 (2019).
51. C. Y. Wang, T. Herr, P. Del'Haye, A. Schliesser, J. Hofer, R. Holzwarth, T. W. Hänsch, N. Picqué, and T. J. Kippenberg, "Mid-infrared optical frequency combs at 2.5 μm based on crystalline microresonators," Nat. Commun. **4**, 1345 (2013).
52. M. A. Tran, D. Huang, and J. E. Bowers, "Tutorial on narrow linewidth tunable semiconductor lasers using Si/III-V heterogeneous integration," APL Photon. **4**, 111101 (2019).

53. M. Li, L. Chang, L. Wu, J. Staffa, J. Ling, U. A. Javid, S. Xue, Y. He, R. Lopez-rios, T. J. Morin, H. Wang, B. Shen, S. Zeng, L. Zhu, K. J. Vahala, J. E. Bowers, and Q. Lin, "Integrated Pockels laser," Nat. Commun. **13**, 5344 (2022).
54. C. Op De Beeck, F. M. Mayor, S. Cuyvers, S. Poelman, J. F. Herrmann, O. Atalar, T. P. McKenna, B. Haq, W. Jiang, J. D. Witmer, G. Roelkens, A. H. Safavi-Naeini, R. Van Laer, and B. Kuyken, "III/V-on-lithium niobate amplifiers and lasers," Optica **8**, 1288–1289 (2021).
55. E. S. Magden, N. Li, M. Raval, C. V. Poulton, A. Ruocco, N. Singh, D. Vermeulen, E. P. Ippen, L. A. Kolodziejski, and M. R. Watts, "Transmissive silicon photonic dichroic filters with spectrally selective waveguides," Nat. Commun. **9**, 3009 (2018).
56. S. Molesky, Z. Lin, A. Y. Piggott, W. Jin, J. Vucković, and A. W. Rodriguez, "Inverse design in nanophotonics," Nat. Photonics **12**, 659–670 (2018).
57. J. Lim, A. A. Savchenkov, E. Dale, W. Liang, D. Eliyahu, V. Ilchenko, A. B. Matsko, L. Maleki, and C. W. Wong, "Chasing the thermodynamical noise limit in whispering-gallery-mode resonators for ultrastable laser frequency stabilization," Nat. Commun. **8**, 8 (2017).
58. M. A. Tran, C. Zhang, T. J. Morin, L. Chang, S. Barik, Z. Yuan, W. Lee, G. Kim, A. Malik, Z. Zhang, J. Guo, H. Wang, B. Shen, L. Wu, K. Vahala, J. E. Bowers, H. Park, and T. Komljenovic, "Extending the spectrum of fully integrated photonics to submicrometre wavelengths," Nature **610**, 54–60 (2022).